INTERNATIONAL JOURNAL FOR NUMERICAL METHODS IN FLUIDS
Int. J. Numer. Meth. Fluids 2008; **57**:653–675
Published online 28 April 2008 in Wiley InterScience (www.interscience.wiley.com). DOI: 10.1002/fld.1763

Fluid–structure interaction in lower airways of CT-based lung geometries

Wolfgang A. Wall*,† and Timon Rabczuk

Chair for Computational Mechanics, Technical University of Munich, Boltzmannstr. 15, 85748 Garching, Germany

SUMMARY

In this study, the deformability of airway walls is taken into account to study airflow patterns and airway wall stresses in the first generations of lower airways in a real lung geometry. The lung geometry is based on CT scans that are obtained from *in vivo* experiments on humans. A partitioned fluid–structure interaction (FSI) approach, realized within a parallel in-house finite element code, is employed. It is designed for the robust and efficient simulation of the interaction of transient incompressible Newtonian flows and (geometrically) non-linear airway wall behavior. Arbitrary Lagrangian–Eulerian-based stabilized tetrahedral finite elements are used for the fluid and Lagrangian-based 7-parametric mixed/hybrid shell elements are used for the airway walls using unstructured meshes due to the complexity of the geometry. Airflow patterns as well as airway wall stresses in the bronchial tree are studied for a number of different scenarios. Thereby, both models for healthy and diseased lungs are taken into account and both normal breathing and mechanical ventilation scenarios are studied. Copyright © 2008 John Wiley & Sons, Ltd.

Received 29 August 2007; Revised 31 October 2007; Accepted 4 December 2007

KEY WORDS: lung; FSI; CT scan; Dirichlet–Neumann partitioning

1. INTRODUCTION

Airflow in the lung is of high interest in pulmonary medicine. For example, airflow patterns and the resulting particle and aerosol depositions play a key role in the pharmaceutic industry. They are also of interest in intensive-care medicine when patients have to be mechanically ventilated. We are interested in airflow patterns and stress distributions in airway walls of mechanically ventilated patients, especially those with acute lung injuries such as acute respiratory distress syndrome and

*Correspondence to: Wolfgang A. Wall, Chair for Computational Mechanics, Technical University of Munich, Boltzmannstr. 15, 85748 Garching, Germany.
†E-mail: wall@lnm.mw.tum.de

Contract/grant sponsor: German Science Foundation (DFG); contract/grant number: WA 1521/8

acute lung injury. Up to now, it is still not clear how to ventilate these patients and the mortality rate of patients with acute lung injuries is quite high, i.e. around 50%.

Most existing numerical studies on airflow patterns in the respiratory system were performed with idealized geometries such as the Weibel [1] or Horsfield *et al.* [2] models, Asgharian and Anjilvel [3], Balashazy and Hoffmann [4], Comer *et al*. [5, 6], Kimbell *et al.* [7], Liu *et al.* [8, 9], Yu *et al.* [10, 11], Zhang and Kleinstreuer [12] and Zhang *et al.* [13, 14]. Only few studies are based on 'real', i.e. based on 3D imaging, airway geometries [15–17]. Almost all studies, both with artificial and real geometries, do not take airway deformations and fluid–structure interaction (FSI) effects into account [16–22]. FSI studies in lower airway geometries, including complex phenomena such as closure and reopening of collapsable tubes, were done only in the lower cartilage-free generations of the lung and were restricted to simplified models/geometries and to single bifurcations [23–26].

In former studies (e.g. [27]) we have found that specific geometric features are essential, see also Liu *et al.* [8, 9], Nowak *et al.* [17], and hence that artificial geometries are not sufficient in several aspects. In pure computational fluid dynamics (CFD) studies, as reported in Rabczuk *et al.* [27], we found severe differences in flow characteristics between artificial and real geometries of the bronchial tree. Consequently, the conjecture seems obvious that even small movements of airway walls can play a severe role on airway flow characteristics. Despite the overall movement of the bronchial tree, cross-sectional deformations in the trachea and in the first airway generations are usually rather small. This is mainly due to the fact that in this region airway walls are rather stiff and mainly consist of cartilage. However, as can easily be seen from 4D medical imaging and also confirmed by our medical partners, along with some lung diseases such as chronic obstructive pulmonary disease (COPD) even in the trachea, cross sections even during normal breathing can change quite significantly.

Our final goal is to understand the breathing/ventilation process in the respiratory system in order to develop together with our medical partners a strategy to better ventilate patients, especially those with acute lung injuries. The breathing process governs flow patterns, velocity and flow distributions, stress and strain distributions in the airway walls, etc. In this study, we try to obtain a first insight into FSI effects during this process. *In vivo* boundary conditions are often very hard to specify or measure. Therefore, the employed boundary conditions are sometimes non-physiological for this initial study. Nevertheless, the adopted model will allow helpful insights. Later on more realistic models will be studied, e.g. taking into account the actual composition of airway walls or pressure differences inside and outside the airway walls. One could in the future also use registration techniques and inverse analysis along with 4D medical imaging.

The computation of FSI problems requires the solution of the coupled fluid and solid underlying governing equations. FSI problems are coupled problems with kinematical and dynamical coupling conditions at the fluid–structure interface. There are two major approaches to solve a coupled FSI problem. In the monolithic approach, all field equations of the FSI problem—i.e. fluid, solid and often also mesh motion—are solved at the same time [28, 29]. Some drawbacks of monolithic approaches are size and conditioning of the system of equations and often missing modularity of the code. Partitioned approaches treat the fluid and the solid domains separately. In each cycle, information has to be transferred from the fluid to the solid and *vice versa*. Various partitioned approaches have been developed, ranging from weakly coupled staggered schemes [30–32] to iterative or strong coupling schemes [33–44]. Strong coupling schemes are particularly needed for stability reasons [45] in many biomechanics problems. The linearized system of equations is solved independently in the solid and fluid domains. The major advantage of this approach is that

DOI: 10.1002/fld

the solvers for the solid and fluid domains can be handled separately, which makes the method very flexible. The major drawback is a slight increase in computation time since additional iterations between the fluid and solid domains are necessary. Other drawbacks for very specific types of problems are discussed in Küttler *et al.* [37]. In the fluid domain, we assume Newtonian fluids under transient incompressible flow conditions. Owing to the complex geometries considered here, tetrahedral finite elements based on an arbitrary Lagrangian–Eulerian (ALE) description of motion are used. In the solid domain, we employ 7-parametric triangular shell elements, Bischoff and Ramm [46] and Bischoff *et al.* [47], which represent the airway walls.

We use a partitioned approach that is based on a non-overlapping non-conforming iterative Dirichlet–Neumann substructuring scheme [36, 40, 44]. The coupling approach prescribes fluid velocities at the coupling interface of the fluid domain and applies the resulting forces to the coupling interface of the structural domain. Essential for robustness and efficiency of the coupling algorithm are the applied acceleration schemes for the iterative process [36, 40]. For all numerical examples in this paper, the Aitken acceleration has been employed. An ALE formulation is employed in order to account for the temporal deformation of the fluid domain. Thus, the fluid mesh is adjusted to the structural deformation during the solution process. The ALE mesh is deformed by an elastic body analogy interpolation according to an algorithm as described, e.g. in [48, 49].

We will present FSI studies in a four-generation lower airway model of CT scan-based lung geometries. The CT scans are obtained from *in vivo* experiments on humans and pigs at different times of the breathing cycle. The data were acquired from the Department of Radiology and the Division of Medical and Biological Informatics of the German Cancer Research Center Heidelberg. The paper is organized as follows: the following section discusses modeling aspects along with the corresponding governing equations. Computational approaches for the individual fields as well as for the coupled problem are given next. Finally, we will present results in the bronchial tree under normal breathing conditions and mechanical ventilation.

2. MODELING AND GOVERNING EQUATIONS

2.1. Airway walls

The configuration of the airway walls is fairly complex and varies at different generations. The trachea consists of C-shaped cartilaginous rings connected by smooth muscles. The cartilage mainly governs the stiffness of the airway walls. In the lower airways, the cartilage becomes disconnected and the airway walls are softer. In the bronchioli at around generation 13, the cartilage disappears completely. For small strain, elastin fibers mainly contribute to the stiffness. Collagen fibers are folded in the undeformed configuration and contribute to the stiffness only under large deformations. The glands, smooth muscle cells, nerves, ground substance, etc. have a much smaller stiffness than elastin fibers and cartilage and hence do not significantly contribute to the stiffness of the airway walls. It is also well known that the human tissue behaves visco-elastic and non-linear. Since we expect only small strains and due to lack of experimental data, we assume the airway walls to behave linear elastic, which seems to be fair for first studies. The assumption of small strains will be verified in our numerical simulations. However, we will take large deformations, i.e. geometric non-linearities, into account. The development of more complex material models will be a topic of future investigations.

DOI: 10.1002/fld

It is well known that arterial walls are prestressed when they are load free. McKay *et al.* [50] studied the prestressing of excised (load-free) airways of different generations and species. Therefore, the airways were opened in longitudinal direction and the opening angles were measured. If the airways were prestressed, large opening angles would be measured due to the stress relaxation. McKay *et al.* [50] found that the results are species dependent. Very small up to no opening angles were obtained for human and porcine lungs, whereas large opening angles were obtained for sheep and rabbit lungs. This indicates that human and porcine lungs are stress free under load-free conditions. Hence, no prestressing conditions have to be taken into account in our airway wall model. We also would like to note that the observations made in McKay *et al.* [50] partially contradict earlier observations in Han and Fung [51] who looked at excised canine and porcine lungs.

The governing non-linear equation for the airway walls is the linear momentum equation given by

$$\rho^{\mathrm{S}}\ddot{\mathbf{d}} = \nabla_0 \cdot (\mathbf{F}\cdot\mathbf{S}) + \rho^{\mathrm{S}}\mathbf{f}^{\mathrm{S}} \quad \text{in } \Omega^{\mathrm{S}} \tag{1}$$

where $\mathbf{d}$ are the displacements, ρ^{S} and $\mathbf{f}^{\mathrm{S}}$ represent the density and body force, respectively, the superscript S denotes the solid domain and the superscript dot denotes material time derivatives. A Lagrangian formulation will be employed in the solid domain. For the employed St Venant–Kirchhoff type of material, the second Piola–Kirchhoff stress tensor $\mathbf{S}$ is related to the Green–Lagrangian strains $\mathbf{E}$ with the consistent tangent operator $\mathbf{C}$ via

$$\mathbf{S} = \mathbf{C} : \mathbf{E} \tag{2}$$

with

$$\mathbf{E} = \tfrac{1}{2}(\mathbf{F}^{\mathrm{T}}\cdot\mathbf{F} - \mathbf{I}) \tag{3}$$

where $\mathbf{F} = \mathbf{I} - \nabla_0\mathbf{d}$ represents the deformation gradient and the index 0 indicates that partial derivatives are taken with respect to material coordinates $\mathbf{X}$. As mentioned above within this paper we will account for geometrical non-linearities but we will assume the material to be linear elastic. Since it is extremely difficult to obtain even one-dimensional stress–strain curves for real lung tissue or components of the airway walls in general, this assumption seems to be fair. The thickness of the airway walls is assumed to be 1.65 mm in all generations. Mainly based on cartilage, the effective Young's modulus is chosen as $E = 9\,\mathrm{MPa}$. We note that the material parameters are first patient dependent and second subjected to a severe scatter. Therefore, we tested different combinations of material parameters for selected configurations but we will present results only for the above-mentioned material parameters.

2.2. *Airway flow*

We assume a Newtonian fluid under unsteady incompressible flow conditions. The underlying governing equation is the Navier–Stokes equation formulated on time-dependent domains:

$$\left.\frac{\partial \mathbf{u}}{\partial t}\right|_{\chi} + (\mathbf{u} - \mathbf{u}^{\mathrm{G}})\cdot\nabla\mathbf{u} - 2\nu\nabla\cdot\boldsymbol{\varepsilon}(\mathbf{u}) + \nabla p = \mathbf{f}^{\mathrm{F}} \quad \text{in } \Omega^{\mathrm{F}} \tag{4}$$

$$\nabla\cdot\mathbf{u} = 0 \quad \text{in } \Omega^{\mathrm{F}} \tag{5}$$

where $\mathbf{u}$ are the velocities, p is the pressure, $\mathbf{u}^{\mathrm{G}}$ is the velocity of the grid, a superscript F denotes the fluid domain and ∇ denotes partial derivatives with respect to the spatial coordinates $\mathbf{x}$, $\nu = \mu/\rho^{\mathrm{F}}$

DOI: 10.1002/fld

is the kinematic viscosity with viscosity μ and fluid density ρ^{F}; $\mathbf{f}^{\mathrm{F}}$ is the body force. The kinematic pressure is represented by p where $\bar{p}=p\rho^{\mathrm{F}}$ is the physical pressure within the fluid field. The balance of linear momentum (4) refers to a deforming ALE frame of reference denoted by $\boldsymbol{\chi}$ where the geometrical location of a mesh point is obtained from the unique mapping $\mathbf{x}=\varphi(\boldsymbol{\chi},t)$. The stress tensor of a Newtonian fluid is given by

$$\boldsymbol{\sigma}^{\mathrm{F}}=-\bar{p}\mathbf{I}+2\mu\boldsymbol{\varepsilon}(\mathbf{u}) \tag{6}$$

with the compatibility condition

$$\boldsymbol{\varepsilon}(\mathbf{u})=\tfrac{1}{2}(\nabla\mathbf{u}+\nabla\mathbf{u}^{\mathrm{T}}) \tag{7}$$

where $\boldsymbol{\varepsilon}$ is the rate of deformation tensor.

2.3. Boundary conditions

The initial and boundary conditions in the fluid domain are

$$\begin{aligned}\mathbf{u}(t=0)&=\mathbf{u}_0 \quad \text{in } \Omega^{\mathrm{F}}\\ \mathbf{u}&=\hat{\mathbf{u}} \quad \text{on } \Gamma^{\mathrm{F}}_{\mathrm{D}}\\ \boldsymbol{\sigma}\cdot\mathbf{n}&=\hat{\mathbf{h}}^{\mathrm{F}} \quad \text{on } \Gamma^{\mathrm{F}}_{\mathrm{N}}\end{aligned} \tag{8}$$

where $\mathbf{n}$ denotes the normal to the fluid boundary $\Gamma^{\mathrm{F}}=\Gamma^{\mathrm{F}}_{\mathrm{D}}\cup\Gamma^{\mathrm{F}}_{\mathrm{N}}$, $\Gamma^{\mathrm{F}}_{\mathrm{D}}\cap\Gamma^{\mathrm{F}}_{\mathrm{N}}=\emptyset$, where $\Gamma^{\mathrm{F}}_{\mathrm{D}}$ is the Dirichlet boundary and $\Gamma^{\mathrm{F}}_{\mathrm{N}}$ is the von Neumann boundary; $\hat{\mathbf{h}}^{\mathrm{F}}$ are the prescribed tractions.

We study healthy and diseased/damaged lungs under normal breathing and mechanical ventilation. For normal breathing conditions, a tidal volume of $2l$ is assumed, which is a reasonable assumption for moderate activity conditions. For mechanical ventilation, experimental data from the respirator are available. There are two strategies to apply boundary conditions. First, velocity inflow conditions at the trachea and constant (uniform and non-uniform for healthy and diseased lungs, respectively) pressure outflow conditions at all outflow boundaries can be applied under inspiratory flow conditions. Then, for the exhalation cycle, the mass flow at the outlets is imposed as velocity inflow boundary conditions where the same profile as for the inspiration is assumed. Alternatively, a pressure time history can be applied at the outlets such that the desired tidal volume is obtained. For the case of normal breathing, the pressure time history at the outlets would be sinusoidal, negative at inspiration and positive at expiration as it occurs in 'reality'. The advantage is that inspiration and expiration can be handled quite naturally within one computation. The difficulty is to calibrate the boundary conditions such that the desired tidal volume is obtained, which is an iterative procedure. We note that due to the deformable airway structure, care has to be taken when Dirichlet 'inlet' boundary conditions are applied under expiration.

The boundary conditions under normal breathing conditions are shown in Figure 1 for one breathing cycle which lasts 4 s, i.e. 2 s inspiration and 2 s expiration. We assume a parabolic inlet boundary velocity profile although the boundary conditions at the trachea are probably more complex, see, e.g. Ma and Lutchen [16].

For the imposition of the boundary conditions under mechanical ventilation, we used the data from the respirator. In the experiments, the patients were ventilated with a positive end expiratory pressure (PEEP) of 5 mbar. The tidal volume was 400 ml and the ratio between inspiration time and expiration time $I:E=1:2$ where an inspiration cycle was 1 s. Mechanical ventilation was

DOI: 10.1002/fld

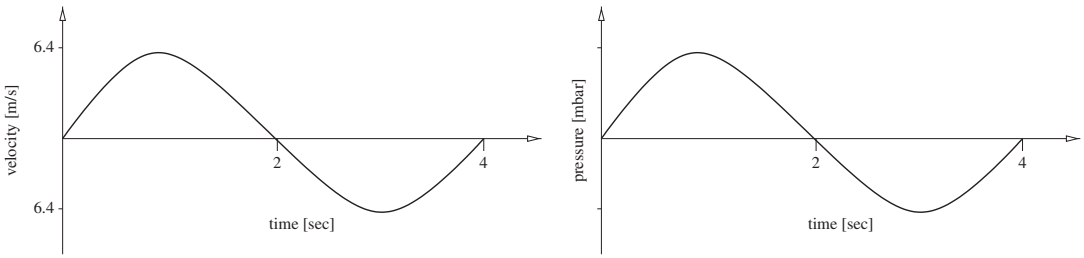

Figure 1. Sinusoidal boundary conditions for normal breathing.

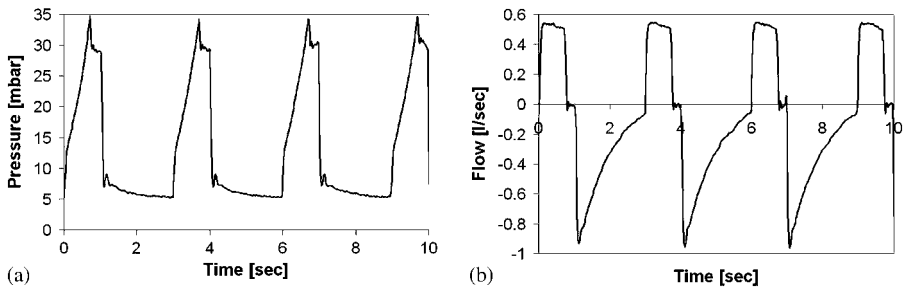

Figure 2. (a) Pressure time history and (b) flow time history of the respirator for the mechanically ventilated lung [52].

performed volume controlled. The pressure time history for one breathing cycle and the corresponding flow time history is shown in Figure 2. These curves were recorded during mechanical ventilation for patients in the ICU [52]. We tested uniform and non-uniform boundary conditions at the outlets. For the case of non-uniform boundary conditions, we set the pressure consistently at all outlets of the right lobe of the lung twice and three times as high as on the left lobe. This should model a diseased lung where a higher stiffness and resistance is expected in the damaged parts of the lung.

The initial and boundary conditions in the solid domain are

$$\begin{aligned} \mathbf{d}(t=0) &= \mathbf{d}_0 \quad \text{and} \quad \dot{\mathbf{d}}(t=0) = \dot{\mathbf{d}}_0 \quad \text{in } \Omega^{\mathrm{S}} \\ \mathbf{d} &= \hat{\mathbf{d}} \quad \text{on } \Gamma^{\mathrm{S}}_{\mathrm{D}} \\ \mathbf{S}\cdot\mathbf{n} &= \hat{\mathbf{h}}^{\mathrm{S}} \quad \text{on } \Gamma^{\mathrm{S}}_{\mathrm{N}} \end{aligned} \tag{9}$$

where $\Gamma^{\mathrm{S}}_{\mathrm{D}}$ and $\Gamma^{\mathrm{S}}_{\mathrm{N}}$ denote the Dirichlet and Neumann partitions of the structural boundary, respectively, with $\Gamma^{\mathrm{S}} = \Gamma^{\mathrm{S}}_{\mathrm{D}} \cup \Gamma^{\mathrm{S}}_{\mathrm{N}}$, $\Gamma^{\mathrm{S}}_{\mathrm{D}} \cap \Gamma^{\mathrm{S}}_{\mathrm{N}} = \emptyset$ and $\hat{\mathbf{d}}$ and $\hat{\mathbf{h}}^{\mathrm{S}}$ denote the prescribed Dirichlet and Neumann values.

The airway walls were fixed at the inlet, i.e. at the top of the trachea. The rest of the lung was allowed to move freely. The surrounding tissue and potential pressure differences that hamper the

DOI: 10.1002/fld

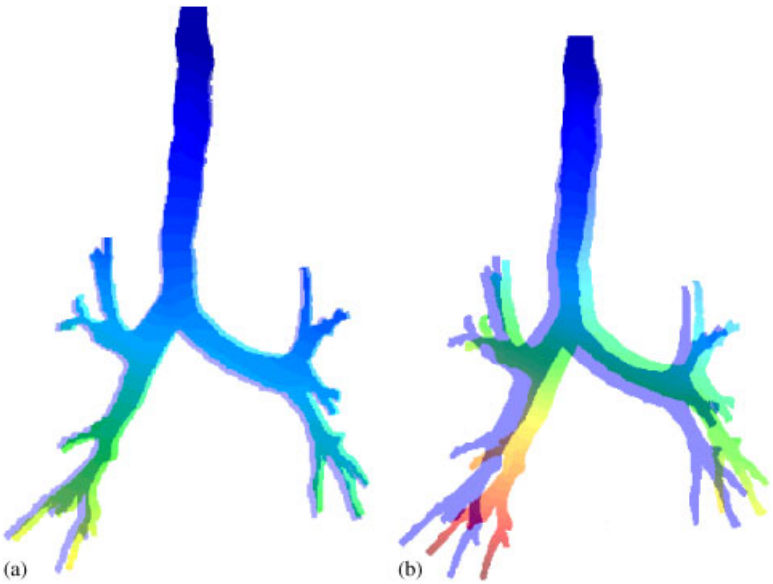

Figure 3. Deformation of the lung under mechanical ventilation at different times during the respiration cycle: (a) 0.2 s and (b) 0.9 s.

movement of the lung were not taken into account in this study. A deformation plot of the lung under mechanical ventilation at different times during the respiration cycle is shown in Figure 3 exemplarily for a mechanically ventilated lung.

3. COMPUTATIONAL APPROACHES

3.1. Computational fluid and solid dynamics

Owing to the complex geometry, the Navier–Stokes equations (4) and (5) in the fluid domain are discretized in space by equal-order linear tetrahedral elements with GLS-type stabilization [53–55]. Details of the discretization of the ALE formulation of the Navier–Stokes equations by means of stabilized finite elements are given in Förster *et al.* [48]. Implicit one-step-θ and BDF2 schemes are used to discretize this set of equations in time. The occurring non-linearities are dealt with Newton or fixed-point-like iteration schemes [49]. The generalized minimal residual iterative solver with ILU preconditioner, which is available within the open-source package AZTEC [56], is used in the fluid domain.

Spatial discretization of the airway walls is done through mixed/hybrid triangular elements based on a 7-parameter shell formulation [46, 47]. This system is solved using the non-linear version of the 'generalized-α method' of Chung and Hulbert [57] along with consistent linearization and a Newton–Raphson iterative scheme.

DOI: 10.1002/fld

3.2. Computational FSI

As stated in the Introduction, the partitioned solution approach is based on a domain decomposition that separates the fluid and the solid. The 'wet' surface of the solid acts here as a natural coupling interface Γ_{FSI} across which displacement and traction continuity at all discrete time steps has to be fulfilled:

$$\mathbf{d}_\Gamma(t)\cdot\mathbf{n}=\mathbf{r}_\Gamma(t)\cdot\mathbf{n} \quad \text{and} \quad \mathbf{u}_\Gamma(t)\cdot\mathbf{n}=\mathbf{u}_\Gamma^{\mathrm{G}}(t)\cdot\mathbf{n}=\left.\frac{\partial\mathbf{r}_\Gamma(t)}{\partial t}\right|_\chi\cdot\mathbf{n} \tag{10}$$

$$\boldsymbol{\sigma}_\Gamma^{\mathrm{S}}(t)\cdot\mathbf{n}=\boldsymbol{\sigma}_\Gamma^{\mathrm{F}}(t)\cdot\mathbf{n} \tag{11}$$

where $\mathbf{r}$ are the displacements of the fluid mesh and $\mathbf{n}$ is the unit normal on the interface. Satisfying the kinematic continuity leads to mass conservation at Γ_{FSI}, satisfying the dynamic continuity yields conservation of linear momentum and energy conservation finally requires to simultaneously satisfy both continuity equations. The algorithmic framework of the partitioned FSI analysis is discussed in detail elsewhere, Küttler and Wall [36], Mok and Wall [40] and Wall *et al.* [44].

The Dirichlet–Neumann partitioning with the fluid domain acting as Dirichlet partition with prescribed velocities $\mathbf{u}_\Gamma$ and the structure domain acting as Neumann partition loaded with interface forces $\mathbf{f}_\Gamma$ are particularly suited for partitioned FSI solutions, at least from an implementational point of view. A Dirichlet–Neumann coupling algorithm with synchronous time discretization [36, 40, 44] and block Gauss–Seidel iteration using Aitken-style relaxation is considered here. For stability reasons strong coupling schemes are essential for these kinds of problems as has been shown in the analysis in Förster *et al.* [45]. Let $(\cdot)_{\mathrm{I}}$ and $(\cdot)_\Gamma$ denote variables or coefficients in the interior of a subdomain Ω^j and on the coupling interface Γ_{FSI}, respectively, while a vector without any of the subscripts I and Γ comprises degrees of freedom on the entire subdomain including interior and interface.

To highlight the coupling behavior, the following outline abbreviates the non-linear field equation for solid and fluid, respectively, with the symbolic systems

$$\mathbf{A}^{\mathrm{S}}\mathbf{d}^{\mathrm{S}}=\mathbf{f}^{\mathrm{S}} \quad \text{and} \quad \mathbf{A}^{\mathrm{F}}\mathbf{u}^{\mathrm{F}}=\mathbf{f}^{\mathrm{F}} \tag{12}$$

In every time step the subsequent calculations have to be performed.

1. Transfer the latest structure displacements $\mathbf{d}^{\mathrm{S}}_{\Gamma_{\mathrm{FSI}},i+1}$ to the fluid field, determine the appropriate fluid velocities at the interface $\mathbf{u}^{\mathrm{S}}_{\Gamma_{\mathrm{FSI}},i+1}$ (satisfying the geometric conservation law) and calculate the fluid domain deformation.
2. Solve for the inner fluid velocities and pressures $\mathbf{u}^{\mathrm{F}}_{\mathrm{I},i+1}$

$$\mathbf{A}^{\mathrm{F}}_{\mathrm{II}}\mathbf{u}^{\mathrm{F}}_{\mathrm{I},i+1}=\mathbf{f}^{\mathrm{F}}_{\mathrm{Iext}}-\mathbf{A}^{\mathrm{F}}_{\mathrm{I}\Gamma_{\mathrm{FSI}}}\mathbf{u}^{\mathrm{S}}_{\Gamma_{\mathrm{FSI}},i+1} \tag{13}$$

3. Find the fluid forces at the interface Γ_{FSI}

$$\mathbf{f}^{\mathrm{F}}_{\Gamma_{\mathrm{FSI}},i+1}=\mathbf{A}^{\mathrm{F}}_{\Gamma_{\mathrm{FSI}}\mathrm{I}}\mathbf{u}^{\mathrm{F}}_{\mathrm{I},i+1}+\mathbf{A}^{\mathrm{F}}_{\Gamma_{\mathrm{FSI}}\Gamma_{\mathrm{FSI}}}\mathbf{u}^{\mathrm{S}}_{\Gamma_{\mathrm{FSI}},i+1} \tag{14}$$

4. Solve for the structural displacements

$$\begin{bmatrix}\mathbf{A}^{\mathrm{S}}_{\Gamma_{\mathrm{FSI}}\Gamma_{\mathrm{FSI}}} & \mathbf{A}^{\mathrm{S}}_{\Gamma_{\mathrm{FSI}}\mathrm{I}}\\ \mathbf{A}^{\mathrm{S}}_{\mathrm{I}\Gamma_{\mathrm{FSI}}} & \mathbf{A}^{\mathrm{S}}_{\mathrm{II}}\end{bmatrix}\begin{bmatrix}\tilde{\mathbf{d}}^{\mathrm{S}}_{\Gamma_{\mathrm{FSI}},i+1}\\ \mathbf{d}^{\mathrm{S}}_{\mathrm{I},i+1}\end{bmatrix}=\begin{bmatrix}\mathbf{f}^{\mathrm{S}}_{\Gamma_{\mathrm{FSI}}\,\mathrm{ext}}-\mathbf{f}^{\mathrm{F}}_{\Gamma_{\mathrm{FSI}},i}\\ \mathbf{f}^{\mathrm{S}}_{\mathrm{Iext}}\end{bmatrix} \tag{15}$$

DOI: 10.1002/fld

5. Relax the interface displacement

$$\mathbf{d}^{\mathrm{S}}_{\Gamma_{\mathrm{FSI}},i+1} = \omega_i \tilde{\mathbf{d}}^{\mathrm{S}}_{\Gamma_{\mathrm{FSI}},i+1} + (1-\omega_i)\mathbf{d}^{\mathrm{S}}_{\Gamma_{\mathrm{FSI}},i} \tag{16}$$

The iteration finishes when the error of the interface displacement $\tilde{\mathbf{d}}^{\mathrm{F}}_{\Gamma_{\mathrm{FSI}},i+1}$ is sufficiently small.

4. RESULTS

The calculations were carried out with the parallel in-house research code *baci* [58, 59] on parts of a 54-node Opteron cluster with two 2.6 GHz processor nodes and 4 GB memory per node using InfiniBand for the network communication. The parallelization was done using message passing interface taking advantage of distributed memory.

4.1. Background information for result presentation

4.1.1. Lung geometry. The bronchial tree of the upper airways was obtained from CT scans of human and porcine lungs under *in vivo* conditions. Therefore, CT scans were prepared under normal breathing and mechanical ventilation at different times. The images were segmented from the Division of Medical and Biological Informatics of the University of Heidelberg by a region-growing technique and the surface of the bronchial tree was obtained by a 3D-skeleton method [60] from a system based on Medical Imaging Interaction Toolkit, see Wolf *et al.* [61]. The surface model of the bronchial tree was stored in stereolithography format (.stl). The surface was then smoothed by a Gauss filter. The outlets of the airways were cut perpendicular to the center line of the airways to facilitate the imposition of boundary conditions. For the fluid, an unstructured Eulerian tetrahedral finite element mesh was then generated from the surface model. For the solid, triangular Lagrangian shell elements were generated from the surface model that are non-conforming to the fluid mesh. The ALE mesh coincided with the Eulerian fluid mesh. We refined the mesh from 110 000 up to 520 000 fluid elements and 50 000–295 000 shell elements, respectively, until the calculated mass flow rate was within a tolerance of 1%. The stl model used as initial mesh for the simulation was the CT-based model at the beginning of the inspiration cycle. The models at other time steps can be used in comparison with the deformed configuration of the bronchial tree in the numerical simulation.

4.1.2. Flow phenomena and measures. In this study, flow patterns and flow distributions are of interest since they play a major role in the damage process of the lung tissue. It is expected that stress concentrations occur at flow peaks with high secondary flow intensities. The secondary flow intensity ξ at certain cross sections can be evaluated by

$$\xi = \frac{\int_A \bar{v}_s \, \mathrm{d}A}{\int_A \bar{v}_p \, \mathrm{d}A} \tag{17}$$

where A is the cross-sectional area, $\bar{v}_s = \sqrt{v_{s1}^1 + v_{s2}^2}$ is the mean secondary velocity, v_{s1} and v_{s2} are the velocity components perpendicular to the axial flow direction and $\bar{v}_p$ is the amplitude of the axial velocity.

DOI: 10.1002/fld

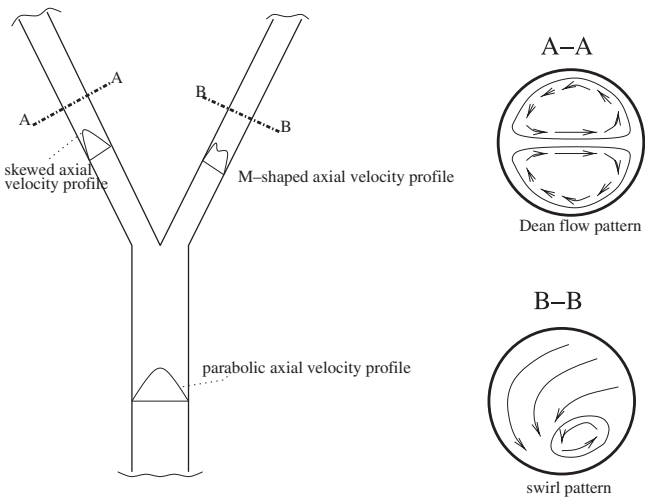

Figure 4. Typical axial and secondary airflow patterns in the lung.

Numerical studies on the bifurcation flow of lung models consistently identified different types of secondary flow pattern such as Dean-flow or swirl-flow pattern (Figure 4). Parabolic, skewed and M-shaped flow patterns were typically observed in the axial direction depending on the Reynolds number. While parabolic-flow patterns characterize low Reynolds number flows, M-shaped axial flow patterns were observed for high Reynolds number flows. Studies on symmetrical Weibel models revealed a Dean-flow pattern in the daughter tube while a skewed swirl pattern was observed in the grandchild tube, see, e.g. Comer *et al.* [5, 6] and Nowak *et al.* [17] although we know that the flow patterns in real lungs are more complex.

It is well known that the flow distribution in the healthy human lung is uniform and it is obvious that the flow distribution for diseased and damaged lungs become non-uniform. The influence of the flow distribution on the flow patterns and stress transmission is not clear. In our computations we will refer to the normalized mass flow [ml/mm^2] which is measured at every outlet and then divided by the cross-sectional area at the corresponding outlet.

4.2. Normal breathing

At inspiration, the trachea exhibits a strong primary flow in the axial direction. There is barely secondary flow present and there is strong off-axis flow due to the geometric asymmetry. The flow is nearly parabolic up to the primary bronchi. After the first flow divider, a secondary Dean flow is observed in the right main bronchus that is strongly asymmetric (Figure 6(a)). In the left main bronchus the secondary flow is skewed towards the bottom wall (Figure 6(b)); for the tube definitions, see Figure 5. While the axial flow in the left bronchus exhibits a skew pattern towards the inner wall close to the next flow divider, the right main bronchus shows an M-shape (Figure 7). The right main bronchus is shorter than the left main bronchus and bifurcates into two secondary bronchi. The right main bronchus bifurcates into three secondary bronchi. In the airways G2.3, G2.4, G2.5, a secondary flow swirl pattern is present (Figure 6(c) and (d)). The 'total' flow pattern

DOI: 10.1002/fld

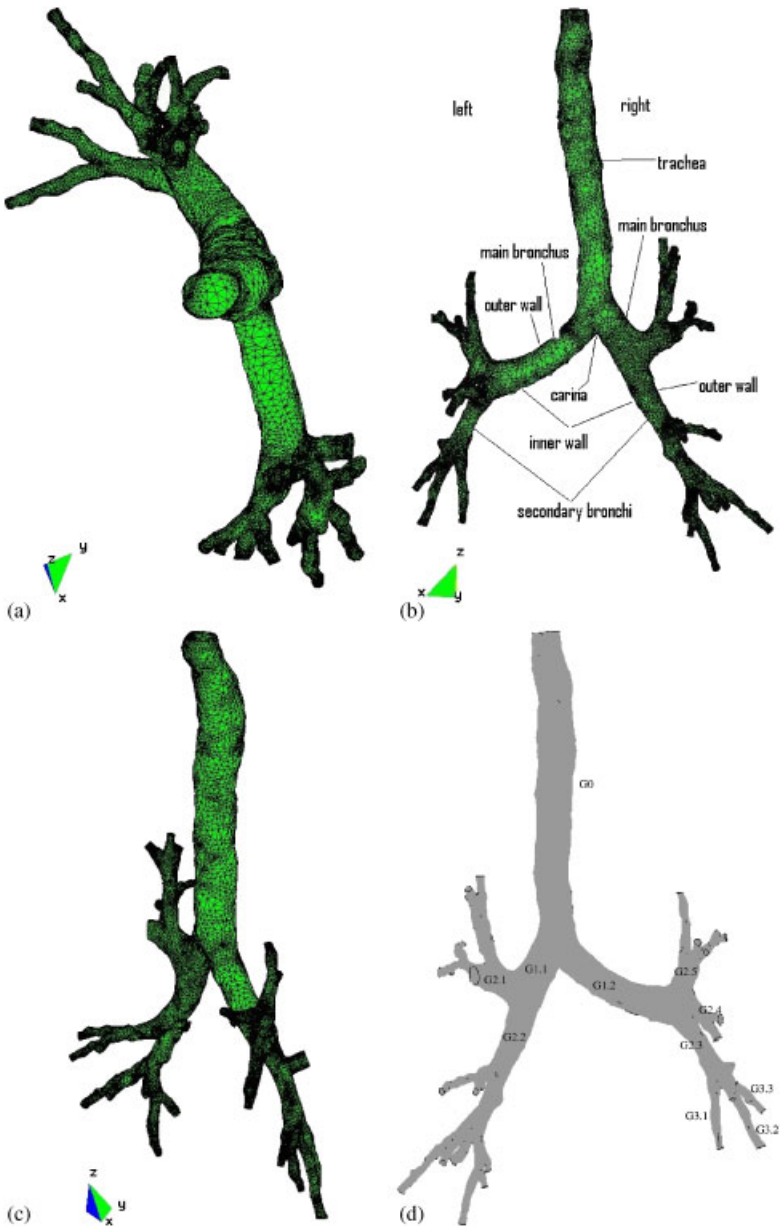

Figure 5. Tube definitions for the human bronchial tree (only tubes that will be considered are numerated).

at peak flow rate in the bronchial tree is shown in Figure 8 for two different points of view. As can be seen, the flow distribution looks relatively homogenous.

The expiratory flow differs from the inspiratory flow. The flow does not split at the flow divider, but the streams join from the daughter tubes, so that near the flow divider the velocity profiles

DOI: 10.1002/fld

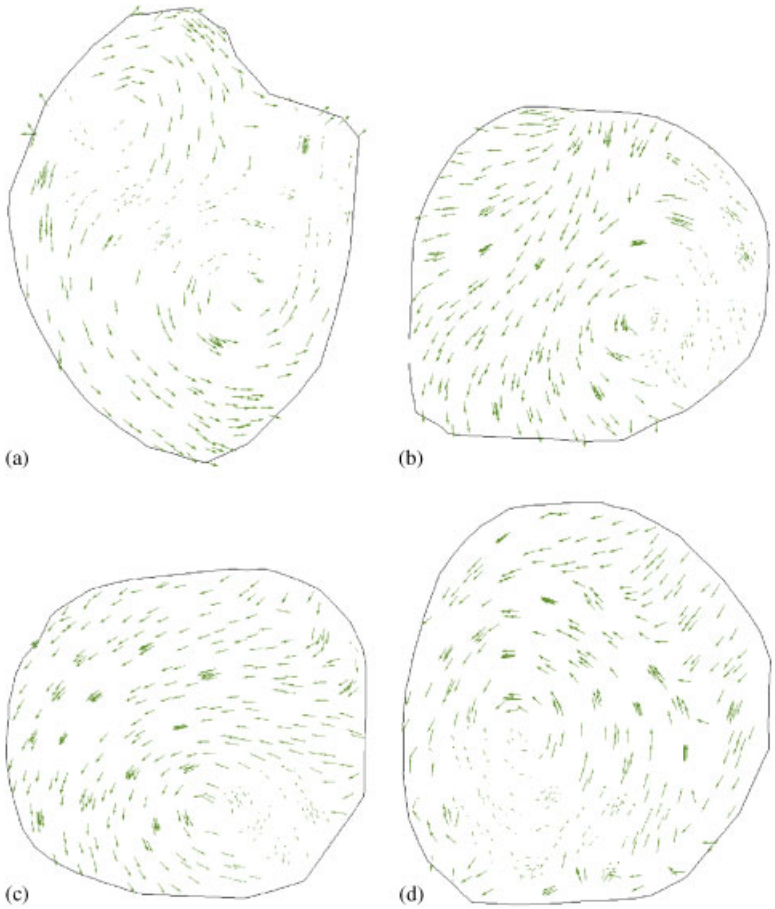

Figure 6. Secondary airflow pattern in the human lung under normal breathing at inspiration, FSI simulation: (a) G1.1; (b) G1.2; (c) G2.3; and (d) G2.5.

in the bifurcation plane have indentations at the center. Generally, in contrast to inhalation flow, expiratory flow features vary only slowly with axial distance. We also note that the flow pattern is similar almost in the entire breathing cycle. Three to four vortices occur in the secondary flow pattern in all tubes. Changes occur at the transition from inspiration and expiration.

In Figure 9, variations of the secondary flow intensity during the inspiration and expiration cycles are illustrated for tubes up to the third generation. Exemplarily, we only show the results of the left bronchial tree. Except at the transition between inspiration and expiration, the secondary flow intensity is more or less uniform. Also the course of the secondary flow intensity over time is similar.

The results obtained from pure CFD simulations are quite different. The secondary airflow patterns of the CFD simulations in the tubes G1.1, G1.2, G2.3 and G2.5 are shown in Figure 10. They are quite different from the airflow patterns of the FSI simulation. For example, while tube G2.3 exhibits a clear secondary swirl-flow pattern in the FSI simulation, a Dean flow is present

DOI: 10.1002/fld

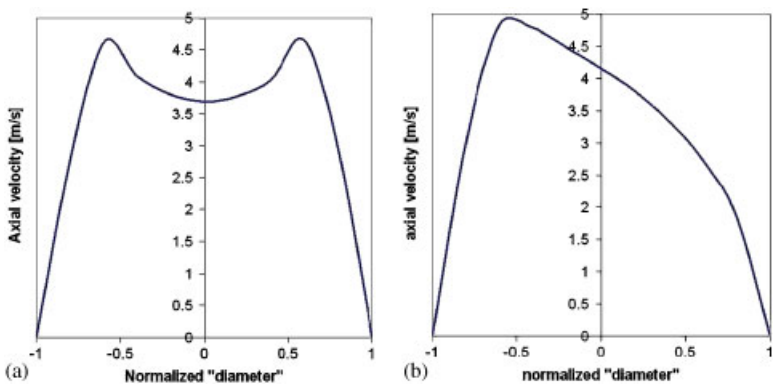

Figure 7. Airflow pattern under normal breathing conditions at inspiratory peak flow rate for the FSI simulation at (a) G1.1 and (b) G1.2.

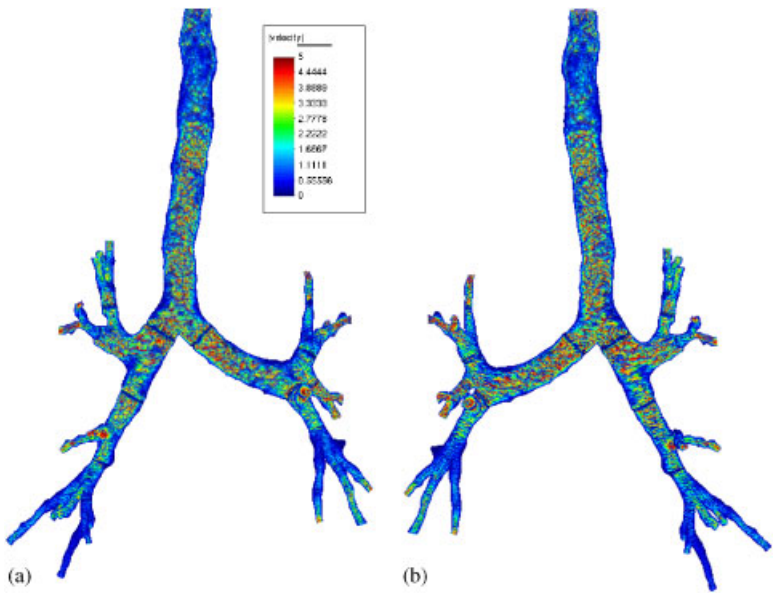

Figure 8. Airflow in the human lung under normal breathing at inspiratory peak flow rate for two different viewpoints.

in the CFD simulation. The secondary airflow intensities of the CFD and FSI simulations are slightly different, compare Figure 9(a) and (b) with 9(c) and (d). The deviations become more pronounced with distance from the inlets. For example, we observe up to 20% deviations in the secondary airflow intensities at tube G2.5 under inspiration, the differences in the main bronchi and the trachea are rather marginal.

DOI: 10.1002/fld

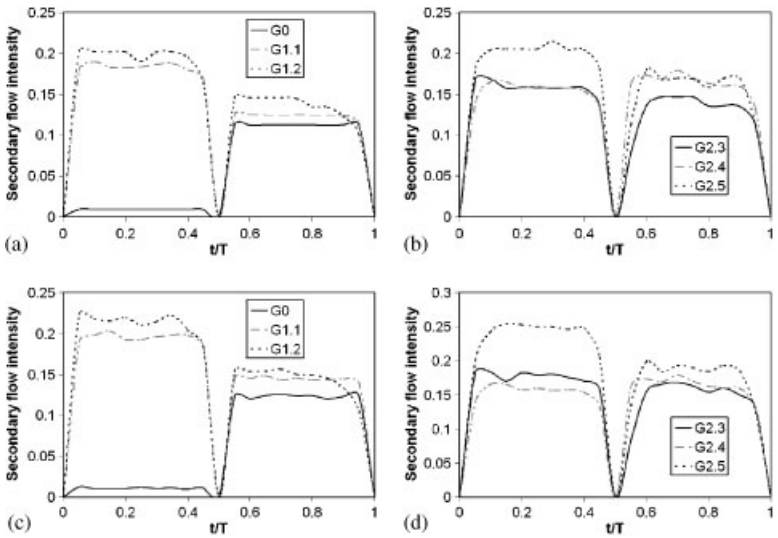

Figure 9. Secondary airflow intensity in the human lung under normal breathing at inspiration and expiration: (a) FSI simulation; (b) FSI simulation; (c) pure GFD simulation; and (d) pure CFD simulation.

The maximum mean Reynolds number $Re = \varrho u D/v$, where ϱ is the density of air, D the tube diameter[‡] and v the dynamic viscosity at peak flow rate under inspiratory flow in the trachea is 4042. The corresponding maximum mean Reynolds numbers in the subsequent bifurcations were as follows: main bronchus 3007, secondary bronchi 2111 and tertiary bronchi 1496. The Wommersley number $\alpha = 0.5D\sqrt{\omega/v}$, where ω is the angular frequency, is often used as a measure for the quasi-steadiness of a flow. It is assumed that the flow is quasi-steady for low Wommersley numbers, e.g. $\alpha < 1$, see Zhang and Kleinstreuer [12]. Jan *et al.* [62] even reported that oscillatory flow at peak flow rate can be assumed as quasi-steady for a Wommersley number $\alpha < 16$. [63] reported about quasi-steady flow conditions in a symmetric model for Wommersley numbers $\alpha < 4.3$. The Wommersley number in the initial configuration does not exceed a value of 2.5 in the trachea and is below a value of 1 in the last generation.

The distribution of the principal tensile stresses in the airway model under inspiratory peak flow rate is shown in Figure 11(a). The largest stresses occur close to the outlets and in the trachea, especially close to the inlet where the trachea shows a slight curvature. The stresses are also largest at bifurcation points, e.g. the carina, Figure 5. At expiratory flow, the stresses are slightly higher in the lower part of the lung. Figure 11(b) shows the stress distribution at expiratory peak flow. The stresses are higher when compared with inspiratory peak flow. We also note that stress concentrations occur where streams are joining. The magnitude of the stresses in the left and right lobes of the lung is similar at same generations for both inspiration and expiration.

The flow distribution is relatively balanced under normal breathing as shown in Figure 12(a). The outlets are numerated arbitrarily in the model in ascending order.

[‡]We note that the cross section is not a circle and D is an 'approximated' diameter.

DOI: 10.1002/fld

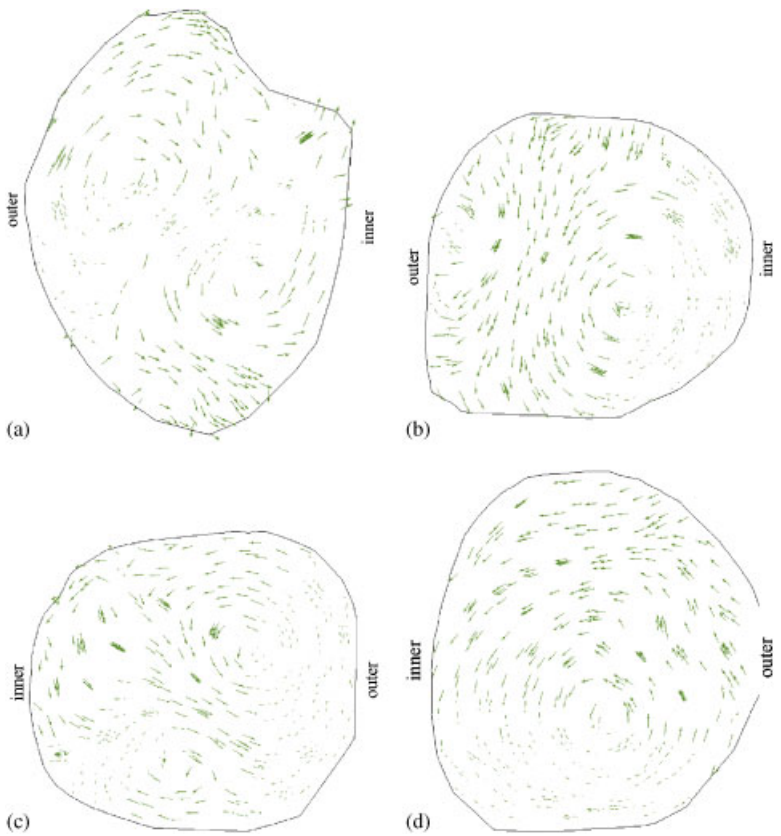

Figure 10. Secondary airflow pattern in the human lung under normal breathing at inspiration, CFD simulation: (a) G1.1; (b) G1.2; (c) G2.3; and (d) G2.5.

4.3. Mechanical ventilation

4.3.1. Healthy lung. The airflow patterns during mechanical ventilation at inspiration are similar to those at normal breathing. The flow quantitatively differs from normal breathing because of the shorter inspiration time, the different pressure/flow time history curves and the smaller tidal volume. The Reynolds number in the entire bronchial tree is lower as under normal breathing. Despite the different breathing patterns, the principal flow pattern is qualitatively quite similar up to generation 2, i.e. in the trachea and in the main bronchi. After the first flow divider, a skew pattern in the secondary flow is present in the two main bronchi, Figure 13(a) and (b); we note that the right main bronchus exhibits a Dean-flow pattern under normal breathing. The axial velocities show an M-shape in tube G1.1 and a skew pattern towards the inner wall in tube G1.2 as under normal breathing. The flow patterns after generation 2 differ from those of normal breathing. Figure 13(c) and (d) shows that the secondary flow pattern in tubes G2.3 and G2.5 are different when compared with their counterparts at normal breathing. The secondary flow intensity at selected cross sections in different generations is shown in Figure 14. Under inspiratory flow,

DOI: 10.1002/fld

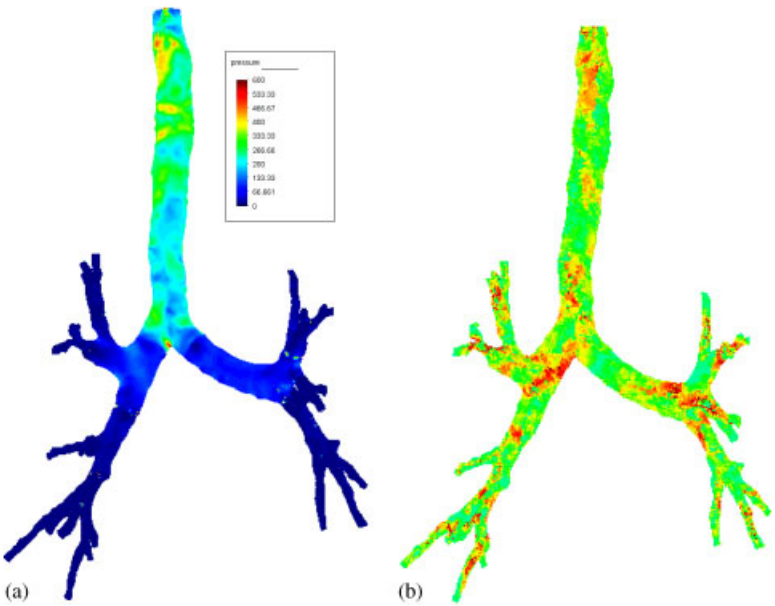

Figure 11. Stress distribution (principal tensile stress) in the airways of the lung under inspiratory and expiratory peak flow rate for normal breathing and the healthy human lung: (a) inspiration—normal breathing and (b) expiration—normal breathing.

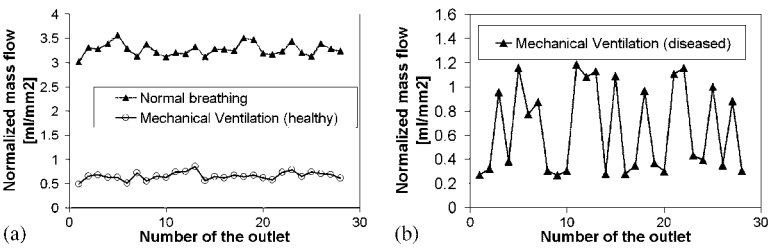

Figure 12. Normalized flow distribution for the human lung at the outlets under normal breathing, mechanical ventilation for the healthy and diseased human lung: (a) healthy lung and (b) diseased lung.

the secondary flow intensity is similar as under normal breathing although the breathing patterns are generally different.

The flow at mechanical ventilation during expiration differs significantly from inspiratory flow as well as from expiratory flow at normal breathing. At the end of the expiration, the pressure is set almost instantaneously to the PEEP pressure of the ventilator that results in a peak flow rate right at the beginning of the expiration cycle. The peak flow at this time is more than twice as high as the maximum peak flow under inspiration. Owing to the sudden pressure drop, the flow deteriorates fast and at the middle of the expiration cycle, most of the air is already expirated. The flow at the beginning of the expiration is unsteady and flow patterns change in time. The secondary flow intensity is significantly higher at this time. Oscillations of the airways can be

DOI: 10.1002/fld

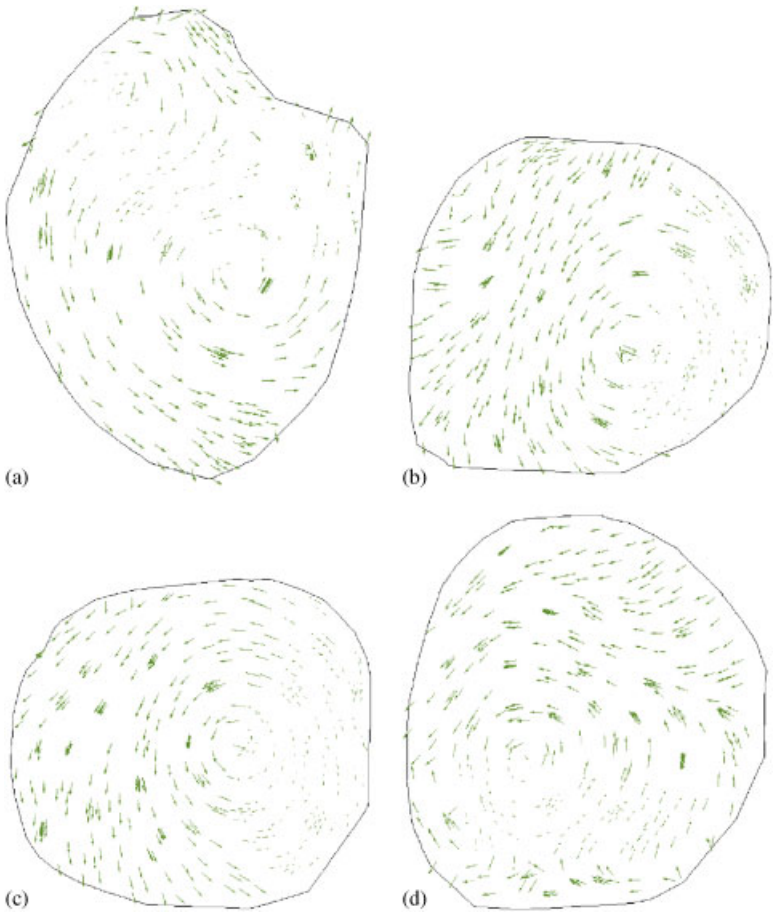

Figure 13. Secondary airflow pattern in the healthy human lung under mechanical ventilation at inspiration, FSI simulation: (a) G1.1; (b) G1.2; (c) G2.3; and (d) G2.5.

observed probably by the large and sudden 'applied' FSI forces at the beginning of the expiration cycle. We expect that these initial oscillations will be reduced when the surrounding tissue and potential differences in the pressure inside and outside the bronchial tree will be included in future simulations.

The magnitude of the stresses at the beginning of the expiration cycle is higher compared with inspiration. At the middle of the expiration cycle, the flow is quasi-steady and the stresses in the airway walls as well as the secondary flow intensity are significantly decreased. The magnitude of the stresses at (selected) certain times are similar at same generations. This was also observed under normal breathing.

The flow distribution remains relatively balanced also under mechanical ventilation and is pretty similar to the flow distribution for normal breathing, Figure 12(a). Because of the significantly smaller tidal volume, the Reynolds numbers under mechanical ventilation are smaller than those under normal breathing conditions. At peak flow rate and inspiratory flow, the mean Reynolds

DOI: 10.1002/fld

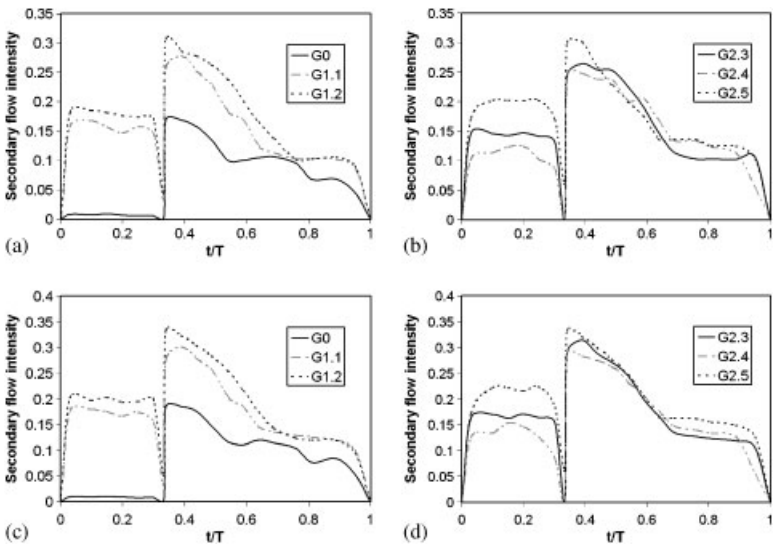

Figure 14. Secondary airflow intensity in the human lung under mechanical ventilation at inspiration and expiration for the healthy lung: (a) FSI simulation; (b) FSI simulation; (c) pure CFD simulation; and (d) pure CFD simulation.

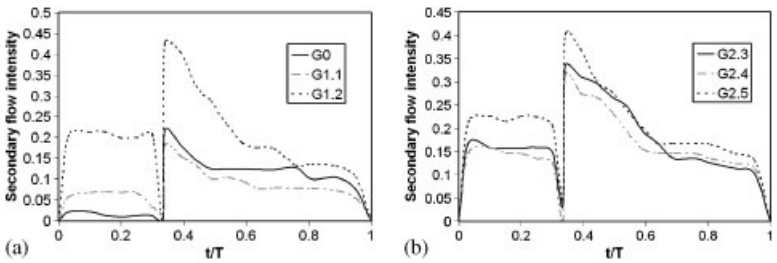

Figure 15. Secondary airflow intensity in the human lung under mechanical ventilation at inspiration and expiration for the diseased lung: (a) FSI simulation and (b) FSI simulation.

numbers at selected cross sections are: trachea 1823, main bronchus 1397, secondary bronchi 1127 and tertiary bronchi 893.

The differences between pure CFD simulations and FSI simulations under mechanical ventilation are very similar as under normal breathing and therefore not further discussed.

4.3.2. Diseased lung. To model a diseased lung, non-uniform outlet boundary conditions are assumed. Therefore, we set the pressure outlet boundary conditions consistently twice and three times higher on the right lobe of the lung compared with the left lobe. This should model a higher stiffness that occurs when parts of the lung in the lower generations are collapsed or highly damaged. We did not consider other configurations of lung damages in the lower parts and leave this for future studies.

DOI: 10.1002/fld

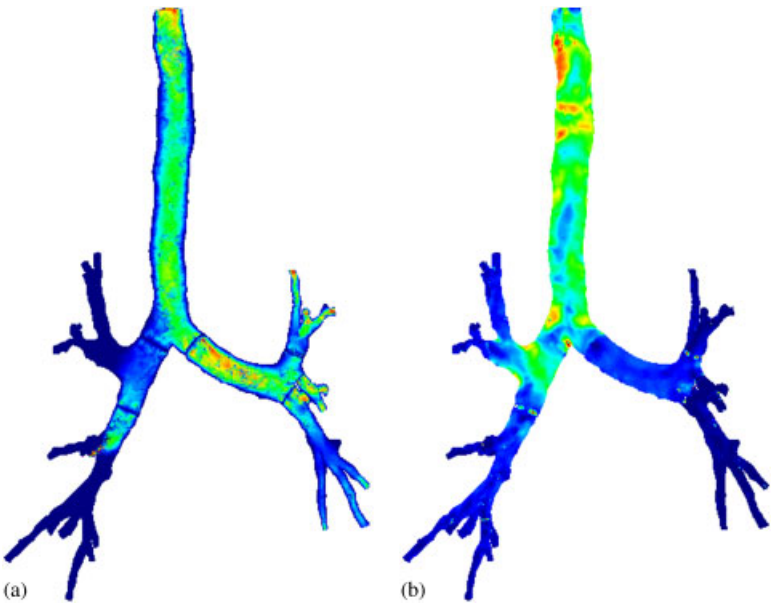

Figure 16. Flow and stress distribution (principal tensile stress) in the airways of the diseased lung under mechanical ventilation: (a) velocity and (b) stress.

The airflow patterns for diseased lungs differ significantly from the airflow patterns for healthy lungs in inspiration as well as in expiration. The flow distribution is no longer uniform because of the different pressure outlet boundary conditions. Only 30% of the air enters the diseased part of the lung, i.e. the right lobe. The normalized flow measured at every outlet is shown in Figure 12.

The expiratory flow is relatively similar to the expiratory flow of the healthy lung under mechanical ventilation. The flow is unsteady at the beginning of expiration with varying secondary flow patterns. The main difference from the healthy lung occurs in the trachea where the strong airflow from the left main bronchus hits the relatively weak airflow from the right main bronchus. The secondary flow intensity at expiration in the well-ventilated left main bronchus is surprisingly lower (Figure 15). We believe that the higher secondary flow in the right lobe of the lung, especially close to the airway walls, is responsible for the non-uniform stress distribution, see Figure 16. Figure 16 also shows the non-uniform flow distribution.

5. CONCLUSION AND FUTURE WORK

We have presented an approach and detailed simulation results of FSI under transient incompressible flow conditions in the lower airways of healthy and diseased lungs based on CT scan geometries for normal breathing conditions as well as for mechanical ventilation. Therefore, we have considered a four-generation model. For the fluid, we have used tetrahedral elements whereas shell elements were employed for the airway walls. FSI was realized based on an ALE formulation and a strongly coupled partitioned approach. The healthy lung is modeled by imposing uniform outlet boundary conditions and non-uniform outlet boundary conditions describe a diseased lung where

DOI: 10.1002/fld

non-resolved parts of the lung are damaged and hence will have a higher stiffness. Linear elastic material behavior is assumed for the airway walls. This is definitely a simplification since it is well known that the components of the airway walls behave non-linear visco-elastic. Since the structure of the airway wall is fairly complex and due to the lack of experimental data, this assumption seems to be justifiable, also because only small changes in the cross-sectional area were observed in the experiments. For patients with chronic obstructive lung disease (COPD), i.e. a disease in the trachea, this assumption does not hold any more.

Moreover, we have neglected effects of the surrounding tissue and potential pressure changes inside and outside the bronchial tree, e.g. under sneezing conditions. In other words, our bronchial tree is able to move freely without any imposed constraints. This will be subject of future investigations.

We found that under inspiratory flow, flow patterns and secondary flow intensities are similar in healthy human lungs, no matter whether we consider normal breathing or mechanical ventilation. The flow distribution remains also homogenous. Under expiratory flow, flow patterns and secondary flow intensities differ between the mechanical ventilated lung and the lung under normal breathing conditions. These differences occur probably due to the sudden pressure drop of the respirator. The flow in diseased lungs differs significantly from the flow in healthy lungs. The flow distribution is non-uniform. Secondary flow intensities are higher in the diseased part of the diseased lung. The magnitude of the stresses for the healthy lung in the left and the right lobes was similar at same generations. This is definitely not the case for diseased lungs.

Compared with former CFD studies of the same lung geometry, we found that the influence of the FSI with respect to the normalized flow distributions, see Figure 12, and secondary flow intensities is moderate. Deviations of these results are within 15%. However, airflow patterns, both axial and in-plane, were quite different between CFD and FSI simulations, especially in lower generations, although the changes in the cross sections are rather minor, i.e. around 2% for cross sections that we checked. The influence of deformable airways will even become more pronounced for COPD patients. More importantly, pure CFD simulations are not capable of capturing the stresses in the lung tissue necessary to assess the damage state of the lung. The assessment and evaluation of damage states in the lung are important in order to develop a patient-specific protective ventilation strategy. The maximum stresses in these preliminary studies were below 300 kPa. However, as mentioned previously, for COPD patients or other patients with lung injuries, higher stresses and larger deformations will occur.

ACKNOWLEDGEMENTS

The support of the German Science Foundation (DFG) under project WA 1521/8 is gratefully acknowledged. We also thank our partners from the Division of Medical and Biological Informatics (Prof. Meinzer), especially Ingmar Wegener, and the Department of Radiology of the German Cancer Research Center Heidelberg (Prof. Kauczor).

REFERENCES

1. Weibel ER. *Morphometry of the Human Lung*. Academic Press: New York, 1963.
2. Horsfield K, Dart G, Olson DE, Filley GF, Cumming G. Models of the human bronchial tree. *Journal of Applied Physiology* 1971; **31**:207–217.
3. Asgharian B, Anjilvel S. A Monte Carlo calculation of the deposition efficiency of inhaled particles in lower airways. *Journal of Aerosol Science* 1994; **25**:711–721.

DOI: 10.1002/fld

4. Balashazy I, Hoffmann W. Deposition of aerosols in asymmetric airway bifurcations. *Journal of Aerosol Medicine* 1995; **26**:273–292.
5. Comer JK, Kleinstreuer C, Zhang Z. Flow structures and particle deposition patterns in double-bifurcation airway models. Part 1. Air flow fields. *Journal of Fluid Mechanics* 2001; **435**:25–54.
6. Comer JK, Kleinstreuer C, Zhang Z. Flow structures and particle deposition patterns in double-bifurcation airway models. Part 2. Aerosol transport and deposition. *Journal of Fluid Mechanics* 2001; **435**:55–80.
7. Kimbell JS, Gross EA, Joyner DR, Godo MN, Morgan KT. Application of computational fluid dynamics to regional dosimetry of inhaled chemicals in the upper respiratory tract of the rat. *Toxicology and Applied Pharmacology* 1993; **121**:253–263.
8. Liu Y, So RMC, Zhang CH. Modeling the bifurcation flow in a human lung airway. *Journal of Biomechanics* 2002; **35**:465–473.
9. Liu Y, So RMC, Zhang CH. Modeling the bifurcation flow in an asymmetric human lung airway. *Journal of Biomechanics* 2003; **36**:951–959.
10. Yu G, Zhang Z, Lessmann R. Computer simulation of the flow field and particle deposition by diffusion in a 3-d human airway bifurcation. *Aerosol Science and Technology* 1996; **25**:338–352.
11. Yu G, Zhang Z, Lessmann R. Fluid flow and particle diffusion in the human upper respiratory system. *Aerosol Science and Technology* 1998; **28**:146–158.
12. Zhang Z, Kleinstreuer C. Transient airflow structures and particle transport in a sequentially branching lung airway model. *Physics of Fluids* 2002; **14**:862–880.
13. Zhang Z, Kleinstreuer C, Kim CS. Cyclic micron-size particle inhalation and deposition in a triple bifurcation lung airway model. *Aerosol Science* 2002; **33**:257–281.
14. Zhang Z, Kleinstreuer C, Donohue JF, Kim CS. Comparison of micro and nano-size particle deposition in a human upper airway model. *Aerosol Science* 2005; **36**:211–233.
15. Cebral JR, Summers RM. Tracheal and central bronchial aerodynamics using virtual bronchoscopy and computational fluid dynamics. *IEEE Transactions on Medical Imaging* 2004; **23**(8):1021–1033.
16. Ma B, Lutchen KR. An anatomically based hybrid computational model of the human lung and its application to low frequency oscillatory mechanics. *Annals of Biomedical Engineering* 2006; in press.
17. Nowak N, Kakade PP, Annapragada AV. Computational fluid dynamics simulation of airflow and aerosol deposition in human lungs. *Annals of Biomedical Engineering* 2003; **31**:374–390.
18. Balashazy I, Heistracher T, Hoffmann W. Air flow and particle deposition patterns in bronchial airway bifurcations: the effect of different cfd models and bifurcation geometries. *Journal of Aerosol Medicine* 1996; **9**:287–301.
19. Calay RK, Kurujareon J, Holdo AE. Numerical simulation of respiratory flow patterns within human lungs. *Respiratory Physiology and Neurobiology* 2002; **130**:201–221.
20. Kim CS, Iglesias AJ. Deposition of inhaled particles in bifurcating airway models: I. Inspiratory deposition. *Journal of Aerosol Medicine* 1989; **2**:1–14.
21. Kim CS, Iglesias AJ, Garcia L. Deposition of inhaled particles in bifurcating airway models: II. Expiratory deposition. *Journal of Aerosol Medicine* 1989; **2**:15–27.
22. Yang XL, Liu Y, So RMC, Yang JM. The effect of inlet velocity profile on the bifurcation copd airway flow. *Computers in Biology and Medicine* 2006; **36**:181–194.
23. Hazel AL, Heil M. Three-dimensional airway reopening: the steady propagation of a semi-infinite bubble into a buckled elastic tube. *Journal of Fluid Mechanics* 2003; **478**:47–70.
24. Heil M. Airway closure: liquid bridges in strongly buckled elastic tubes. *Journal of Biomechanical Engineering* (ASME) 1999; **121**:487–493.
25. Heil M, White JP. Airway closure: surface-tension-driven non-axisymmetric instabilities of liquid-lined elastic rings. *Journal of Fluid Mechanics* 2002; **462**:79–109.
26. White JP, Heil M. Three-dimensional instabilities of liquid-lined elastic tubes—a lubrication theory model. *Physics of Fluids* 2005; **17**:031506s2005d.
27. Rabczuk T, Wall WA, Wegener I, Puderbach M. Computational studies on lower airway flows of human and porcine lungs based on CT-scan geometries for normal breathing and mechanical ventilation. submitted.
28. Heil M. An efficient solver for the fully coupled solution of large-displacement fluid–structure interaction problems. *Computer Methods in Applied Mechanics and Engineering* 2004; **193**:1–23.
29. Hübner B, Walhorn E, Dinkler D. A monolithic approach to fluid–structure interaction using space–time finite elements. *Computer Methods in Applied Mechanics and Engineering* 2004; **193**:2087–2104.
30. Farhat C, van der Zee K, Geuzaine P. Provably second-order time-accurate loosely-coupled solution algorithms for transient nonlinear computational aeroelasticity. *Computer Methods in Applied Mechanics and Engineering* 2006; **195**:1973–2001.

DOI: 10.1002/fld

31. Felippa CA, Park KC, Farhat C. Partitioned analysis of coupled mechanical systems. *Computer Methods in Applied Mechanics and Engineering* 2001; **190**:3247–3270.
32. Piperno S. Explicit/implicit fluid/structure staggered procedures with a structural predictor and fluid subcycling for 2d inviscid aeroelastic simulations. *International Journal for Numerical Methods in Fluids* 1997; **25**:1207–1226.
33. Dettmer WG, Peric D. A computational framework for fluid–structure interaction: finite element formulation and applications. *Computer Methods in Applied Mechanics and Engineering* 2006; **195**:5754–5779.
34. Fernández MÁ, Moubachir M. A Newton method using exact Jacobians for solving fluid–structure coupling. *Computers and Structures* 2005; **83**(2–3):127–142.
35. Gerbeau J-F, Vidrascu M, Frey P. Fluid–structure interaction in blood flows on geometries coming from medical imaging. *Computers and Structures* 2005; **83**:155–165.
36. Küttler U, Wall WA. Fixed-point fluid–structure interaction solvers with dynamic relaxation. *Computational Mechanics* 2007. DOI: 10.1007/s00466-008-0255-5.
37. Küttler U, Förster Ch, Wall WA. A solution for the incompressibility dilemma in partitioned fluid–structure interaction with pure Dirichlet fluid domains. *Computational Mechanics* 2006; **38**:417–429.
38. LeTallec P, Mouro J. Fluid structure interaction with large structural displacements. *Computer Methods in Applied Mechanics and Engineering* 2001; **190**:3039–3067.
39. Matthies HG, Steindorf J. Partitioned strong coupling algorithms for fluid–structure interaction. *Computers and Structures* 2003; **81**:805–812.
40. Mok DP, Wall WA. Partitioned analysis schemes for the transient interaction of incompressible flows and nonlinear flexible structures. In *Trends in Computational Structural Mechanics*, Wall WA, Bletzinger K-U, Schweitzerhof K (eds). 2001.
41. Tezduyar TE. Finite element methods for flow problems with moving boundaries and interfaces. *Archives of Computational Methods in Engineering* 2001; **8**:83–130.
42. Tezduyar TE. Finite element methods for fluid dynamics with moving boundaries and interfaces. *Encyclopedia of Computational Mechanics*. Wiley: New York, 2004.
43. Tezduyar TE, Sathe S, Keedy R, Stein K. Space–time finite element techniques for computation of fluid–structure interactions. *Computer Methods in Applied Mechanics and Engineering* 2006; **195**:2002–2027.
44. Wall WA, Mok DP, Ramm E. Partitioned analysis approach of the transient coupled response of viscous fluids and flexible structures. In *Solids*, *Structures and Coupled Problems in Engineering*, *Proceedings of the European Conference on Computational Mechanics ECCM '99*, Munich, Wunderlich W (ed.). 1999.
45. Förster Ch, Wall WA, Ramm E. Artificial added mass instabilities in sequential staggered coupling of nonlinear structures and incompressible flows. *Computer Methods in Applied Mechanics and Engineering* 2007; **196**: 1278–1293.
46. Bischoff M, Ramm E. Shear deformable shell elements for large strains and rotations. *International Journal for Numerical Methods in Engineering* 1997; **40**:4427–4449.
47. Bischoff M, Wall WA, Bletzinger K-U, Ramm E. Models and finite elements for thin-walled structures. In *Encyclopedia of Computational Mechanics*, Chapter 3, vol. 2, Stein E, De Borst R, Hughes TJR (eds). Wiley: New York, 2004.
48. Förster Ch, Wall WA, Ramm E. On the geometric conservation law in transient flow calculations on deforming domains. *International Journal for Numerical Methods in Fluids* 2006; **50**:1369–1379.
49. Wall WA. Fluid–Struktur-Interaktion mit stabilisierten Finiten Elementen. *Ph.D. Thesis*, Institut für Baustatik, Universität Stuttgart, 1999.
50. McKay KO, Wiggs BR, Pare PD, Kamm RD. Zero-stress state of intra- and extraparenchymal airways from human, pig, rabbit and sheep lung. *Journal of Applied Physiology* 2002; **92**:1261–1266.
51. Han HC, Fung YC. Residual strains in porcine and canine tracheas. *Journal of Biomechanics* 1991; **24**:307–315.
52. Stahl C. Personal communication, unpublished data.
53. Gravemeier V, Wall WA, Ramm E. A three-level finite element method for the instationary, incompressible Navier–Stokes equations. *Computer Methods in Applied Mechanics and Engineering* 2004; **193**:1323–1366.
54. Gravemeier V, Wall WA, Ramm E. Large eddy simulation of turbulent incompressible flows by a three-level finite element method. *International Journal for Numerical Methods in Fluids* 2005; **48**:1067–1099.
55. Hughes TJR, Franca LP, Hulbert GM. A new finite element formulation for computational fluid-dynamics: VIII. The Galerkin/least squares method for advective diffusive equations. *Computer Methods in Applied Mechanics and Engineering* 1989; **73**:173–189.
56. Tuminaro M, Heroux S, Hutchinson SA, Shadid JN. *Official Aztec User's Guide*, Version 2.1, 1999.
57. Chung J, Hulbert GM. A time integration algorithm for structural dynamics with improved numerical dissipation; the generalized-α method. *Journal of Applied Mathematics* 1993; **60**:371–375.

58. Gee M, Ramm E, Wall WA. Parallel multilevel solution of nonlinear shell structures. *Computer Methods in Applied Mechanics and Engineering* 2005; **194**:2285–2707.
59. Küttler U, Wall WA. An approach for parallel fluid–structure interaction on unstructured meshes. In *Recent Advances in Parallel Virtual Machine and Message Passing Interface*, Mohr B, Träff J, Worringer J, Dongarra J (eds). Lecture Notes in Computer Science Series. Springer: Berlin, 2006; 366–373.
60. Schöbinger M, Thorn M, Vetter M, Cardenas CE, Hassenpflug P, Wolf I, Meinzer H-P. Robuste Analyse von Gefässstrukturen auf Basis einer 3D-Skelettierung. *Bildverarbeitung für die Medizin*, 2003; 76–80.
61. Wolf I, Vetter M, Wegner I, Böttger T, Nolden M, Schöbinger M, Hastenteufel M, Kunert T, Meinzer H-P. The medical imaging interaction toolkit (MITK). *Medical Image Analysis* 2005; **9**(6):594–604. Available from: http://dx.doi.org/10.1016/j.media.2005.04.005.
62. Jan DL, Shapiro H, Kamm RD. Some features of oscillatory flow in branching network of tubes. *Journal of Applied Physiology* 1989; **167**:147.
63. Lieber BB, Zhao Y. Oscillatory flow in a symmetric bifurcation airway model. *Annals of Biomedical Engineering* 1998; **26**:821.

DOI: 10.1002/fld